Complex processes in simple ices : laboratory and observational studies of gas-grain interactions during star formation

Öberg, K.I.

8 PHOTODESORPTION OF CO, N$_2$ AND CO$_2$ ICES

A longstanding problem in astrochemistry is how molecules can be maintained in the gas phase in dense inter- and circumstellar regions at temperatures well below their thermal desorption values. Photodesorption is a non-thermal desorption mechanism, which may explain the small amounts of observed cold gas in cloud cores and disk mid-planes. This study aims to determine the UV photodesorption yields and to constrain the photodesorption mechanisms of three astrochemically relevant ices: CO, N$_2$ and CO$_2$. In addition, the possibility of co-desorption in mixed and layered CO:N$_2$ ices is explored. The experimental photodesorption studies are carried out under ultra high vacuum conditions and at astrochemically relevant temperatures (15 – 60 K) using a hydrogen discharge lamp (7–10.5 eV). The ice desorption is monitored by reflection absorption infrared spectroscopy of the ice and simultaneous mass spectrometry of the desorbed molecules. Both the UV photodesorption yield per incident photon and the photodesorption mechanism are highly molecule specific. The CO photodesorbs without dissociation from the surface layer of the ice, and N$_2$, which lacks a dipole allowed electronic transition in the wavelength range of the lamp, has a photodesorption yield that is more than an order of magnitude lower. This yield increases due to co-desorption when N$_2$ is mixed in with, or layered on top of, CO ice. CO$_2$ photodesorbs through dissociation and subsequent recombination from the top 10 layers of the ice. At 15 – 18 K the derived photodesorption yields are $2.7(\pm1.3) \times 10^{-3}$ and $< 2 \times 10^{-4}$ molecules photon^{-1} for pure CO and N$_2$, respectively. The CO$_2$ photodesorption yield is $1.2(\pm0.7) \times 10^{-3} \times (1 - e^{-(x/2.9(\pm1.1))}) + 1.1(\pm0.7) \times 10^{-3} \times (1 - e^{-(x/4.6(\pm2.2))})$ molecules photon^{-1}, where x is the ice thickness in monolayers and the two parts of the expression represent a CO$_2$ and a CO photodesorption pathway, respectively. At higher temperatures, the CO ice photodesorption yield decreases, while that of CO$_2$ increases.

8.1 Introduction

In dark clouds molecules and atoms collide with and stick to cold submicron-sized dust particles, resulting in icy mantles (Léger et al. 1985; Boogert & Ehrenfreund 2004). The ices are subsequently processed by atom or light interactions to form more complex species (Tielens & Hagen 1982; Watanabe et al. 2003; Ioppolo et al. 2008). Observations show that H$_2$O, CO and CO$_2$ are the main ice constituents, with abundances up to 10^{-4} with respect to the total hydrogen density. These molecules are key constituents in the formation of more complex species (Tielens & Charnley 1997), and their partitioning between the grain and gas phase therefore strongly affects the chemical evolution in star- and planet-forming regions (van Dishoeck 2006).

Whether formed on the grains or frozen out from the gas phase, chemical models of cloud cores show that all molecules except for H$_2$ are removed from the gas phase within $\sim 10^9/n_{\mathrm{H}}$ years, where n_{H} is the total hydrogen number density (Willacy & Millar 1998). For a typical cloud core density of 10^4 cm^{-3}, this time scale is much shorter than the estimated age of such regions and thus molecules like CO and CO$_2$ should be completely frozen out. Yet gas-phase molecules, like CO, are detected in these clouds (Bergin et al. 2001, 2002). Cold CO gas is also detected in the midplanes of protoplanetary disks (Dartois et al. 2003; Piétu et al. 2007) where the densities are higher and the freeze-out time scales are even shorter, suggesting the existence of either efficient non-thermal desorption or an efficient mixing process in the disks. Similarly Sakai et al. (2008) have detected cold HCO$_2^+$, tracing gas phase CO$_2$, toward the embedded low-mass protostar IRAS 04368+2557 in L 1527 also referred to as L 1527 IRS. From the high column density and the thin line profile they conclude that the observed CO$_2$ cannot originate from thermal evaporation of ices in the hot inner regions of the envelope. They instead suggest gas phase formation of CO$_2$ to explain their observations, but do not consider non-thermal desorption in the cold envelope as an alternative. HCO$_2^+$ is also detected by Turner et al. (1999) toward several small translucent molecular clouds. They conclude that the observed HCO$_2^+$ can only form through gas phase chemistry for very specific C/O ratios and time spans and that the source of gas phase HCO$_2^+$ may instead be desorbed CO$_2$ ice. Both the CO and CO$_2$ observations may thus be explained by non-thermal desorption of ices, but this has not been quantified to date.

In dense clouds and in outer disks and disk midplanes, desorption must occur non-thermally since the grain temperature is low enough, around 10 K, that thermal desorption is negligible. Suggested non-thermal desorption pathways include photon and cosmic ray induced processes and desorption following the release of chemical energy (Shen et al. 2004; Roberts et al. 2007).The importance of these processes depend both on the intrinsic desorption yields and on the local environment, especially the UV and cosmic ray fluxes. External UV photons from the interstellar radiation field can penetrate into the outer regions of dense clouds and disks and this UV field may be enhanced by orders of magnitude in disks through irradiation by the young star. In addition to direct interaction with ices, cosmic rays and X-rays also produce a UV field inside of the clouds through interaction with H$_2$.

UV photodesorption is therefore possible in most dense astrophysical environments,

but it has been proposed as an important desorption pathway of ices mainly in protoplanetary disks and other astrophysical regions with dense clumps of material and excess UV photons (Willacy & Langer 2000; Dominik et al. 2005). There is however a lack of experimentally determined photodesorption yields for most astrophysically relevant molecules. This has prevented progress in the field and in most models UV photodesorption is simply neglected. Recently we showed that CO photodesorption is an efficient process with a yield of $3(\pm 1) \times 10^{-3}$ photon^{-1} (Öberg et al. 2007b). This is of the same order as H_2O photodesorption, investigated by Westley et al. (1995b,c), though the dependence of the H_2O yield on different parameters remains unclear. The photodesorption of H_2O and benzene in a H_2O dominated ice has also been investigated by Thrower et al. (2008) who only find substrate and matrix mediated desorption processes.

In this study we determine the photodesorption yield of CO_2 and its dependence on ice thickness, temperature, morphology, UV flux and integrated UV flux or fluence as well as UV irradiation time. In addition, we extend the previously reported investigation of CO and N_2 photodesorption to include different temperatures and ice morphologies. From the deduced yield dependencies we constrain the different desorption mechanisms and discuss the astrophysical implications.

8.2 Experiments and their analysis

8.2.1 Experimental details

The experimental set-up (CRYOPAD) is described in detail by Fuchs et al. (2006) and Öberg et al. (2007b). The set-up allows simultaneous detection of molecules in the gas phase by quadrupole mass spectrometry (QMS) and in the ice by reflection absorption infrared spectroscopy (RAIRS), with an angle of incidence of 84°, using a Fourier transform infrared (FTIR) spectrometer. The FTIR covers $1200 - 4000$ cm^{-1} with a spectral resolution of 0.5–1 cm^{-1}.

In the experiments presented here, thin ices of 2.1–16.5 monolayers (ML) are grown with monolayer precision under ultra-high vacuum conditions ($P \sim 10^{-10}$ mbar) at $15 - 60$ K on a gold substrate that is mounted on a He cryostat. All experiments are conducted with the isotopologues ^{13}CO and $^{13}C^{18}O$ (Cambridge Isotope Laboratories 99% and 97% purity, respectively), $^{15}N_2$ (Campro Scientific 98% purity), and $^{13}CO_2$ (Indugas 99% purity) and $^{13}C^{18}O_2$ (ICON Isotopes 96% purity) to avoid contributions from atmospheric contaminations as well as to be able to separate CO and N_2 mass spectrometrically with the QMS. Test experiments show that the isotopologue choices do not affect the experimental outcomes for any of the ices.

Within the uncertainties of the experiment, we also find that there is no difference in the photodesorption yield of 6.5 ML CO_2 ice deposited on top of another 7 ML CO_2 ice (of a different isotopologue), or 7 ML CO_2 on top of 10 ML of H_2O ice, compared with 6–7 ML CO_2 ice deposited directly onto the gold substrate. Since the character of the substrate seems to have no influence on the photodesorption process, all other experiments are carried out with CO_2 ices directly on top of the gold substrate.

145

The ice films are irradiated at normal or 45° incidence with UV light from a broadband hydrogen microwave discharge lamp, which peaks around Ly α at 121 nm and covers 115–170 nm or 7–10.5 eV (Muñoz Caro & Schutte 2003). All photodesorption experiments are performed in the same experimental chamber and the different UV angles of incidence are obtained by rotating the gold substrate. The lamp emission resembles the spectral distribution of the UV interstellar radiation field that impinges externally on all clouds. It is also consistent with the UV radiation produced locally inside clouds by the decay of electronic states of H$_2$, following excitation by energetic electrons resulting from cosmic-ray induced ionization of hydrogen, see e.g. Sternberg et al. (1987).

The 45° and the normal incidence irradiation settings produce the same experimental results, except for a reduced photon flux on the ice in the 45° setting due to geometry. The lamp UV flux is varied between 1.1 and 8.3 $\times 10^{13}$ photons cm^{-2} s^{-1} in the different experiments. The UV flux is monitored during all experiments using the photoelectric effect in a thin gold wire in front of the lamp. Before the start of the experimental run, this gold wire current was calibrated to an absolute flux in a separate set-up by simultaneously measuring the flux with a NIST calibrated silicon diode and the current induced in the gold wire. During the photodesorption experiments the flux onto the ice surface is also estimated by measuring the CO$_2$ photodissociation cross-section several times during the experimental run, at both normal and 45° incidence, and comparing our derived cross sections with the calibrated values in Cottin et al. (2003). This was deemed necessary since the calibration measurements were carried out with normal incidence in the separate set-up, while most experiments used a 45° incidence angle. To prevent photodesorption during these measurements, the CO$_2$ ice is covered with an inert ice layer. We find that in the normal incidence setting the resulting flux using this actiometry method deviates by a factor 0.9-1.4 from the photodiode-calibrated gold-wire results.

Tables 8.1 and 8.2 summarize the experiments in this study. In the CO experiments, the temperature is varied between 15 and 27 K, which is close to its thermal desorption temperature (Öberg et al. 2005). This complements the previous CO photodesorption experiments, which investigated the dependences of photodesorption on lamp flux and ice thickness at 15 K (Öberg et al. 2007b). In three additional experiments the photodesorption yield (or upper limits) of N$_2$ is determined, as well as the changes in CO and N$_2$ ice photodesorption in a CO:N$_2$ ice mixture and in a N$_2$/CO layered ice at 16 K. In the CO$_2$ experiments the temperature is set to 16 – 60 K, the irradiation flux to $1.1 - 8.3 \times 10^{13}$ photons cm^{-2} s^{-1} and the ice thickness to 2.1 – 16.5 ML.

8.2.2 Data analysis

The UV induced ice loss yield during each CO and CO$_2$ experiment is determined by RAIRS of the ice during irradiation. The intensity of the RAIRS profile is linearly correlated with the ice layer thickness of CO and CO$_2$ ice up to ~5 ML, but the RAIRS profile can be used up to 20 ML for analysis as long as the non-linear growth above 5 ML is taken into account (Fig. 8.1). The absolute loss yield in number of molecules lost per incident photon is calculated from the RAIRS intensity loss as a function of UV fluence.

For this calculation it is vital to have good estimates of the CO and CO$_2$ band strengths.

Table 8.1 – Summary of CO and N_2 experiments

No.	Composition	Temp. (K)	Thick. (ML)	UV flux (10^{13} cm^{-2} s^{-1})
1	^{13}CO	15	4	4.7
2	^{13}CO	22	3.5	4.7
3	^{13}CO	27	3.5	4.7
4	$^{13}CO^a$	16	3	4.7
5	$^{15}N_2$	16	4	4.7
6	$^{13}CO{:}^{15}N_2$ mixed	16	4:4	4.7
7	$^{15}N_2/^{13}CO$ layered	16	1/4	4.7

[a]annealed ice (i.e. deposited at 27 K and then cooled down to 16 K)
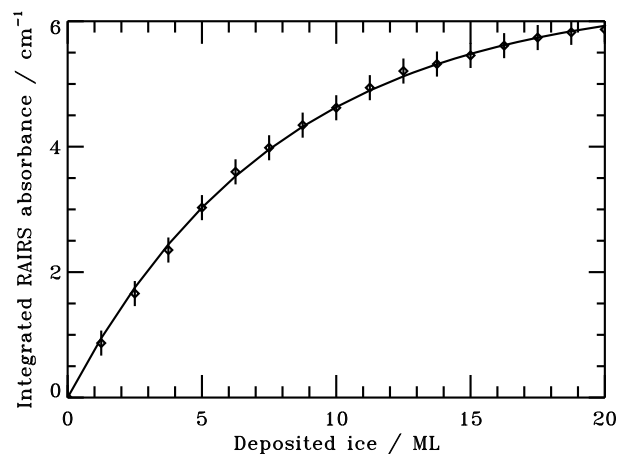

Figure 8.1 – *The integrated absorbance of the $^{13}C^{18}O_2$ stretching band as a function of deposited ice. The fitted exponential function is used to correct for non-linear growth of the integrated absorbance above 5 ML.*

Due to the fact that all ice measurements are done using RAIRS, the ice thickness cannot be estimated from previously determined ice transmission band strengths. Instead the band strength of one ice monolayer is calculated from the observed difference in isothermal desorption from multilayer coverages (constant rate) and monolayer coverages (decreasing rate) as shown in Fig. 8.2. For CO this was done at 31 K and for CO_2 at 76 K. The integrated absorbance of 1 ML is estimated to within 40% from the RAIR spectra at this turning point, which in its turn is used to calculate a band strength relevant for RAIRS. The calculated band strengths are 0.07 and 0.55 cm^{-1} ML^{-1} for CO and CO_2 at their respective desorption temperatures. At 18 K the bands are somewhat weaker at 0.06 and 0.42 cm^{-1} ML^{-1} , respectively. These values are highly set-up specific and they depend on such experimental parameters as mirror settings and should not be used for other purposes. This technique is based on the assumption that the ice is quite flat at the desorption temperature, which was confirmed by the previous CO experiments (Öberg et al. 2007b). For CO, the deduced ice thicknesses agree well (within 20%) with the theoretical

147

Table 8.2 – Summary of CO_2 experiments

No.	Composition	Temp. (K)	Thick. (ML)	UV flux (10^{13} cm^{-2} s^{-1})
1	$^{13}C^{18}O_2$	16	5.5	4.7
2	$^{13}C^{18}O_2$	18	2.1	2.3
3	$^{13}C^{18}O_2$	18	5.5	2.3
4	$^{13}C^{18}O_2$	18	5.6	2.3
5	$^{13}C^{18}O_2$	18	9.0	2.3
6	$^{13}C^{18}O_2$	18	16.5	2.3
7	$^{13}C^{18}O_2$	18	3.9	1.1
8	$^{13}C^{18}O_2$	18	4.7	3.5
9	$^{13}C^{18}O_2$	20	6.2	8.3
10	$^{13}C^{18}O_2$	18	6.5	8.3
11	$^{13}C^{18}O_2$ [a]	18	7.0	2.3
12	$^{13}C^{18}O_2$ [a]	16	4	4.7
13	$^{13}C^{18}O_2$	30	6.2	2.3
14	$^{13}C^{18}O_2$	40	5.8	2.3
15	$^{13}C^{18}O_2$	50	6.7	2.3
16	$^{13}C^{18}O_2$	60	3.3	2.3
17	$^{13}C^{18}O_2$	60	7.4	2.3
18	$^{13}C^{18}O_2$	60	5.8	1.1
19	$^{13}C^{18}O_2$	60	6.2	8.3
20	$^{13}C^{18}O_2$	60	11.0	2.3
21	$^{13}CO_2$	16	3.8	4.7
22	$^{13}CO/^{13}C^{18}O_2$ [b]	18	10/5	2.3
23	$N_2/^{13}C^{18}O_2$ [b]	18	20/5.4	2.3
24	$^{13}C^{18}O_2/CO_2$ [b]	18	6.5/7	2.3
25	$^{13}C^{18}O_2/H_2O$ [b]	18	7/10	2.3

[a] Annealed ice (i.e. deposited at 60 K and then cooled down to 16 or 18 K)
[b] Layered ices

values for our chosen deposition pressure and deposition time (Attard & Barnes 2004). For CO_2, the measured ice thickness is ~30% lower than predicted, probably due to the fact that some of the CO_2 freezes out on the heating shield rather than depositing onto the substrate. Using this method we find that the relative band strengths of CO and CO_2 ice compare well (within 20%) with previously measured transmission band strengths (Hudgins et al. 1993; Gerakines et al. 1996). To convert the band strengths from cm^{-1} ML^{-1} to cm molecule^{-1} a surface density of ~10^{15} molecules cm^{-2} is assumed.

In the case of CO, there is no measurable photodissociation in this wavelength range and the measured photon-induced loss yield is the photodesorption yield (Gerakines et al. 1996; Cottin et al. 2003; Öberg et al. 2007b). Simultaneous QMS measurements of the desorbed CO gas phase molecules allow for the calibration of the QMS signal to an absolute photodesorption yield. The calibrated QMS signal for CO is used to determine the fraction of the CO_2 ice that photodesorbs as CO. It is also used, together with the
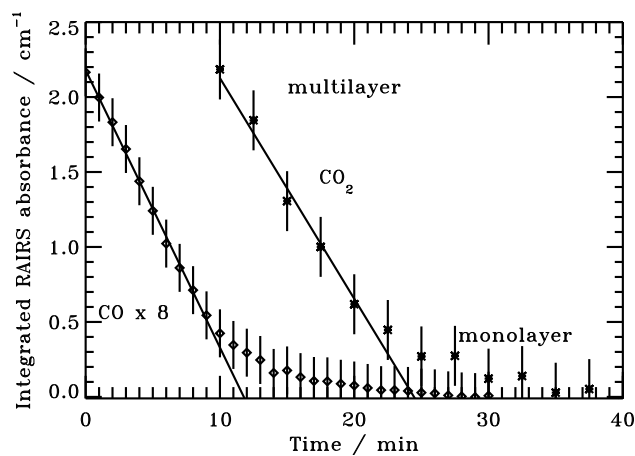
Figure 8.2 – The integrated absorbance of the $^{13}C^{18}O$ and $^{13}C^{18}O_2$ stretching bands as a function of time during isothermal desorption of $\sim$ 5 ML ices at 31 and 76 K, respectively. The linear fits are used to distinguish between the multilayer and monolayer desorption regimes.

measured relative sensitivities of the QMS filament to CO and N_2, to determine the N_2 photodesorption yield. The N_2 photodesorption yield cannot be determined by RAIRS since N_2 has no permanent dipole moment and thus no strong IR feature.

In contrast to CO, CO_2 has only dissociative transitions in the wavelength region of the lamp; a UV photon absorption dissociates CO_2 into CO + O with a quantum yield of up to 98% in the gas phase (Slanger & Black 1978). Hence, UV irradiation induces chemistry as well as desorption (Gerakines et al. 1996). To determine the total photodesorption yield, the ice loss due to desorption must be separated from the conversion of CO_2 into other ice products. This is done by analysis of the RAIR spectra using two different methods: kinetic modeling and mass balance. The first method uses the different kinetics of surface processes, like desorption, and bulk processes, like ice photolysis, to distinguish between the two. Surface desorption from a multilayer ice is expected to be a zeroth order process and the photodesorption yield, which is determined from the derivative of the ice thickness with fluence, should therefore be constant with UV fluence. Photolysis into other species occurs throughout the ice at equal yield, since the ices here are thin enough that optical depth effects can be ignored, and is consequently expected to be a first order process. The contributions of desorption and photolysis to the observed ice loss is then determined by fitting the observed ice thickness versus fluence to the sum of a linear function and an exponential decay function, corresponding to a zeroth and a first order reaction. This method has the advantage that it is not dependent on identifying the photolysis products of CO_2 and it is used to derive photodesorption yields whenever the zeroth and first order curves are separable. This is mainly the case for the high temperature and high fluence experiments.

The mass balance analysis method compares the total ice loss with the simultaneous formation of other species in the ice; the final photodesorption yield is then defined as the loss yield of the original ice minus the formation yield of other carbon-bearing ice species. This is the only method that works for ices that are exposed to low fluences,

149

where the contributions from the zeroth and first order processes cannot be separated. In the CO$_2$ experiments CO, CO$_3$ and O$_3$ are the expected reaction products (Gerakines et al. 1996), with CO dominating. The photodesorption yield is then the CO$_2$ loss yield minus the formation yield of CO and CO$_3$, though as seen below the contribution from CO$_3$ is negligible. This method depends on the relative infrared band strengths of the formed molecules and is thus only accurate in the temperature range where the CO band strengths are measured, i.e. <30 K. As seen below, these two methods agree very well in the few cases where both methods are used to derive photodesorption yields.

The simultaneous mass spectrometry of gas phase molecules during irradiation reveals the nature of the desorbed species. This is limited by the fact that less volatile molecules (e.g. CO$_2$) adsorb onto the heating shield and other semi-cold surfaces inside the experiment before reaching the mass spectrometer. In the case of CO$_2$, only the fractions of the ice that desorb as CO and other volatile species are detected by the QMS. At temperatures above 30 K the conversion factor between QMS detected and desorbed CO changes due to a decrease in cryopumping of CO, which is accounted for when deriving the CO-from-CO$_2$ photodesorption yield. For both CO and CO$_2$, re-condensation onto the actual ice sample after desorption will play a negligible role given the small surface area of the sample and the resulting underestimate of the actual photodesorption will be substantially lower than other sources of inaccuracy.

To summarize, the main sources of uncertainty in these experiments are the photon flux and ice thickness calibrations of ~30% and 40%, respectively. In addition, from repeated experiments, the CO and CO$_2$ experimental results are found to vary with approximately 10% and 25%, respectively. The uncertainty is greater for CO$_2$ than for CO because of the extra steps in deriving the CO$_2$ photodesorption yield. The total uncertainty is ~60% for the CO$_2$ photodesorption yield and ~50% for the CO photodesorption yield. The N$_2$ photodesorption yield uncertainty is somewhat higher due to the larger uncertainty in the QMS measurements.

8.3 Results

8.3.1 CO and N$_2$

The results from photodesorption experiments of pure CO ice at 15 K are reported in Öberg et al. (2007b). The yield presented there is updated here using new ice thickness and lamp flux calibrations; at 15 K the CO photodesorption yield is $(2.7\pm1.3) \times 10^{-3}$ CO molecules per *incident* photon, averaged over the wavelength range of the lamp. The corresponding photodesorption quantum efficiency per *absorbed* UV photon in the surface layer is estimated using the lamp spectrum from Muñoz Caro & Schutte (2003) and the UV spectrum of CO ice from Mason et al. (2006). The UV ice absorption spectrum shows that the CO lines are resolved. The measured absorption spectrum $\int^{UV} A_\lambda^{ice} d\lambda$ is not calibrated to a UV cross section so in our calculation it is assumed that the total UV absorption cross section is the same in the ice as measured in the gas phase $\int^{UV} \sigma_\lambda^{gas} d\lambda$ (Eidelsberg et al. 1992, 1999). The fraction of incident photons that are absorbed in the
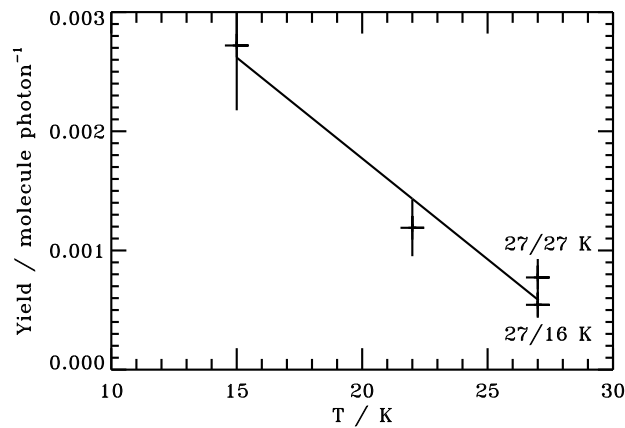
Figure 8.3 – *The CO ice photodesorption yield as a function of ice deposition temperature between 15 and 27 K. The ices are photodesorbed at the deposition temperature except for '27/16 K', where the ice is deposited at 27 K and then cooled down and irradiated at 16 K.*

top monolayer, χ_{abs}, is calculated from

$$\chi_{abs} = \frac{\int^{UV} I_\lambda^{UV-lamp} A_\lambda^{ice} d\lambda}{\int^{UV} I_\lambda^{UV-lamp} d\lambda} \times \frac{\int^{UV} \sigma_\lambda^{gas} d\lambda}{\int^{UV} A_\lambda^{ice} d\lambda} \times N_s \tag{8.1}$$

by cross-correlating the UV-lamp spectrum with the absorption spectrum of CO ice, divided by the total UV flux, $\int^{UV} I_\lambda^{UV-lamp} d\lambda$, and then multiplying with the cross section conversion factor and the amount of molecules in one monolayer, N_s. The resulting absorption fraction is $5.5 \pm 0.2 \times 10^{-3}$, where the uncertainty reflects the error in the gas phase cross section. Comparison with our measured photodesorption yield results in an efficiency of 0.3–0.8 per absorbed photon at 15 K, including both the absorbance and the photodesorption uncertainties.

Figure 8.3 shows that the CO photodesorption yield decreases with ice temperature such that it is almost a factor of three lower at 27 K compared to 15 K. Within this temperature range the CO photodesorption yield is empirically described as linearly dependent on temperature: $2.7 \times 10^{-3} - (T-15) \times 1.7 \times 10^{-4}$ molecules photon^{-1}, where T is temperature in K. An additional experiment, where the ice is deposited at 27 K and then cooled down to 16 K before irradiation, results in a similar desorption yield as when the ice is also desorbed at 27 K. In quantum efficiency terms this corresponds to 0.1–0.3 photodesorption events per absorbed photon in the top ice layer, at 27 K as well as for the annealed ice at 16 K. This indicates that the structure of the ice, rather than the temperature, affects the photodesorption yield. This is further supported by a change in RAIRS profile at 22 and 27 K compared to that at 15 K (Fig. 8.4). Changes in the CO spectra with temperature have been previously reported by e.g. Fuchs et al. (2006). These spectral profiles do not change visibly after a UV fluence of 7×10^{17} photons cm^{-2} when the ices are irradiated at their deposition temperature (not shown). Figure 8.4 also shows the spectral profile of the annealed ice before and after irradiation, which has not changed significantly with cool
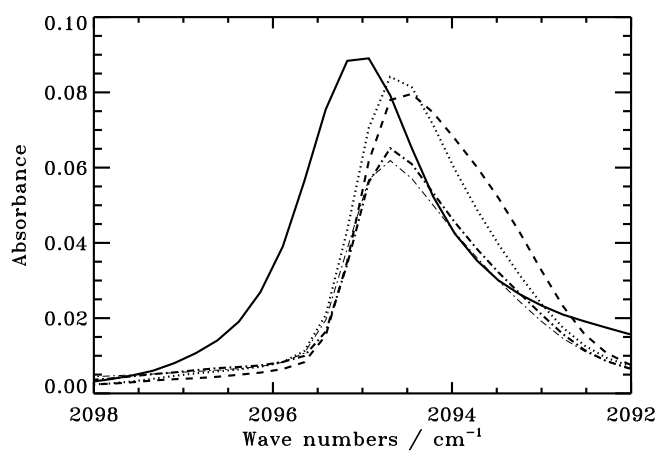
Figure 8.4 – *CO spectra at 15 K (solid), 22 K (dotted), 27 K (dashed), and 16 K after deposition at 27 K (dash dotted), all acquired before irradiation. The figure also shows a spectrum of the annealed ice acquired after a UV fluence of $\sim 7 \times 10^{17}$ photons cm^{-2} (thin dash dotted).*

down, and it has at most slightly shifted toward the 15 K ice spectral profile following irradiation. uncertainties.
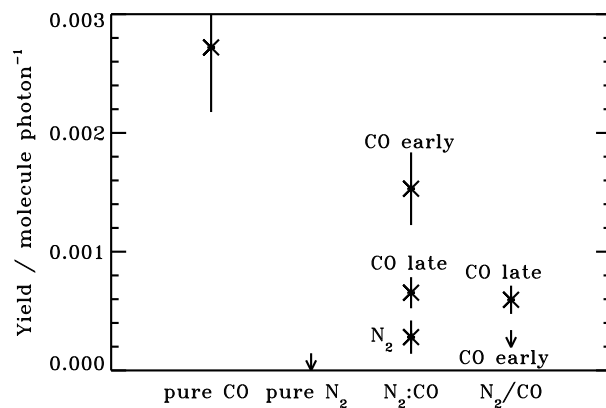

Figure 8.5 – *The CO and N_2 desorption yields at 15/16 Kin 4 ML pure CO and pure N_2 ices, a 4:4 ML mixed ice, and a N_2/CO 1/4 ML layered ice. 'Early' and 'late' marks the CO desorption yield in the beginning of the experiment and after a photon fluence of 8.5×10^{17} cm^{-2}.*

In Öberg et al. (2007b) the N_2 photodesorption yield is constrained to a factor of 10 less than the CO yield at 15 K. With increased sensitivity of the mass spectrometer, N_2 photodesorption is now detected at a yield of 1.8×10^{-4} N_2 molecules photon^{-1} or a factor of 15 lower than the CO photodesorption yield. This value has a factor of two uncertainty, mainly due to the uncertainty in the conversion of the mass spectrometer signal into an ice desorption yield. This measured yield is real, but because of continuous freeze-out of ~0.1 ML H_2O ice per hour the N_2 ice contains an H_2O impurity. A typical experiment lasts 5–6 hours resulting in a maximum 12% contamination level (a significant fraction of the

adsorbed H_2O molecules photodesorbs themselves during the irradiation experiments). This probably affects the measured photodesorption yield due to co-desorption of ices and thus the measured yield should be used as a strict upper limit of pure N_2 photodesorption.

In two additional experiments a $CO:N_2$ mixture 4:4 ML and a N_2/CO layered 1/4 ML ice are irradiated at 16 K. Figure 8.5 shows that in the ice mixture experiment the N_2 desorption yield more than doubles compared to pure N_2 ice, while the CO desorption yield decreases by a factor of 2–4 compared to pure CO ice during the experiment. After a fluence of $\sim 2 \times 10^{17}$ photons cm^{-2} the CO desorption yield is 50% of the photodesorption yield of pure CO. This is expected in a 1:1 mixture, since only 50% of the surface is covered with CO. With increasing fluence the CO desorption yield decreases such that it is only 25% of the yield of pure CO photodesorption after 8.5×10^{17} photons cm^{-2}. This can only be understood if the N_2 molecules desorb with a lower yield than the CO molecules, resulting in a decreasing CO surface concentration with UV fluence. In the layered experiment the CO photodesorption yield is initially below the detection limit. After a UV fluence of 8.5×10^{17} photons cm^{-2} the yield increases to 25% of the pure CO photodesorption yield. The N_2 mass spectrometry signal does not reach equilibrium in the layered experiment, but the desorption yield seems to be at a similar level as in the mixed ice.

8.3.2 CO_2

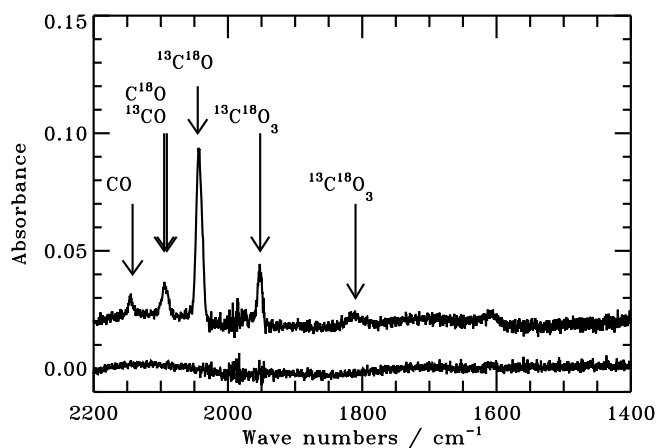### 8.3.2.1   Derivation of the total photodesorption yield

Figure 8.6 – $^{13}C^{18}O_2$ ice at 18 K before (bottom) and after (top) a UV fluence of 5×10^{17} photons cm^{-2}. Some of the original CO_2 ice is photolyzed into CO, CO_3 (ν_1 at 1953 cm^{-1} and $2\nu_4$ in Fermi resonance with ν_1 at 1810 cm^{-1}).

To use the mass balance method to calculate the CO_2 photodesorption yield, it is necessary to constrain which molecules are formed during irradiation. Figure 8.6 shows the spectra of an 18 K, 9 ML thick CO_2 ice before and after a UV fluence of 5×10^{17} photons cm^{-2}. The only formed molecules are CO and CO_3, though O_3 formation cannot

153

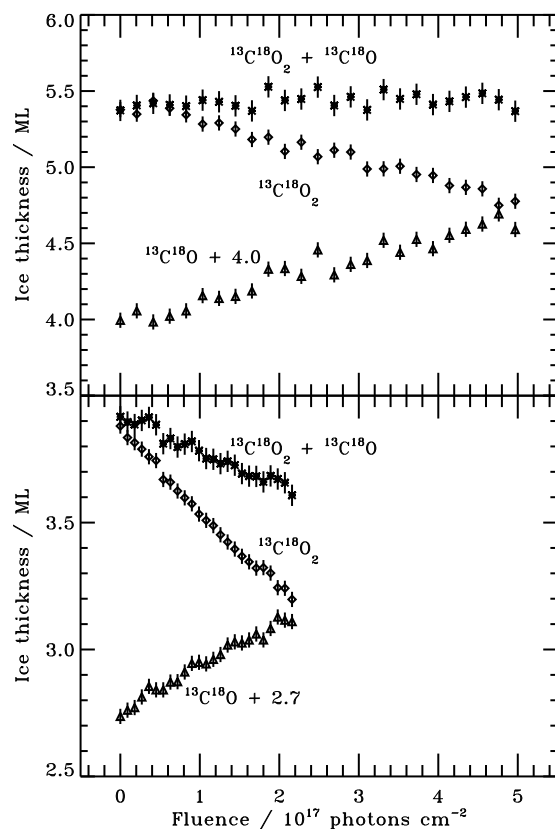**Figure 8.7** – Top: the $^{13}C^{18}O_2$ ice thickness (diamonds) in a 18 K, 20/5.4 ML $N_2/^{13}C^{18}O_2$ layered ice as a function of fluence, plotted together with the formed $^{13}C^{18}O$ ice (triangles) and the constant calculated total ice thickness (stars). Bottom: the decreasing total ice thickness with UV fluence in an 18 K, 3.9 ML icet. The error bars indicate the relative uncertainty in the integrated absorbance (converted to a ML scale) of the RAIRS features within each experiment. This is also the case for similar plots throughout the paper

be excluded since the strong ν_3 $^{18}O_3$ band around 1040 cm^{-1} is outside of the range of the detector. This is in agreement with Gerakines et al. (1996), who found CO, CO_3 and small amounts of O_3 after irradiating CO_2 with a similar fluence. The line positions are taken from Brewer & Wang (1972), Moll et al. (1966) and Gerakines & Moore (2001). The weak band around 1605 cm^{-1} cannot be unambiguously assigned. The lack of other features in the spectra from e.g. carbon-suboxides put strict upper limits on the formation of such molecules to a fraction of a percentage of the original CO_2 ice. This is consistent with the experiments of Gerakines & Moore (2001) where no carbon-suboxides was detected after UV irradiation of pure CO_2 ice. In addition Temperature Programmed Desorption (TPD) experiments following irradiation show that ~10% of the original ice is photolyzed into CO, ~1% into O_2 or O_3 and ~0.1% into C_2. From this we infer that more than 99% of the carbon budget is bound up in CO_2, CO and CO_3 during the experiment.

The CO_2 and CO abundances during each experiment are calculated from their derived band strengths. The CO_3 band strengths have not been measured, however, and can only be crudely estimated. This will introduce a large uncertainty into the mass balance
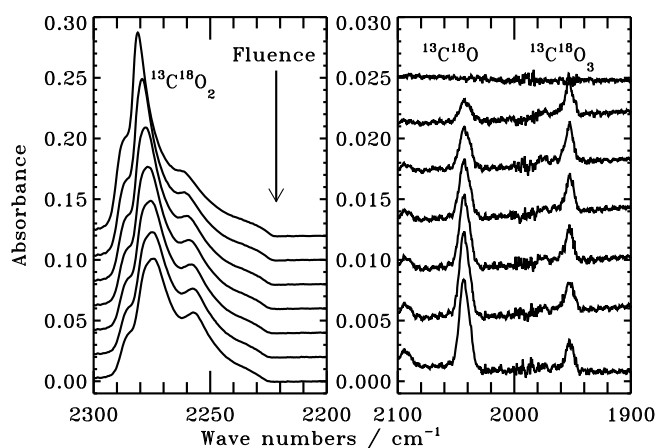
Figure 8.8 – RAIR spectra of the $^{13}C^{18}O_2$ stretching band at 2280 cm^{-1}, the $^{13}C^{18}O$ stretching band at 2045 cm^{-1} and the $^{13}C^{18}O_3$ ν_1 band at 1950 cm^{-1} acquired before irradiation of a 11 ML $^{13}C^{18}O_2$ ice at 18 K and then after every 8.3×10^{16} photons cm^{-2}.

calculations if CO_3 is formed at significant abundances. Figure 8.7 shows the calculated CO_2 and CO ice thicknesses as a function of fluence for a layered 20/5.4 ML N_2/CO_2 ice. The ice cover hinders desorption and the result is that 10% of the original CO_2 is photolyzed into CO. The fact that the lost CO_2 is perfectly compensated for by the formed CO ice shows that CO_3 is not a significant photolysis product. The lack of photodesorption in the layered experiment (top Fig. 8.7) is contrasted with the observed photodesorption of a 3.9 ML bare CO_2 ice (bottom Fig. 8.7).

The CO_3 abundance is also estimated independently by employing its only likely formation path and the fact that CO_3 reaches its final level within $\sim 5 \times 10^{16}$ photons cm^{-2} in all experiments (exemplified in Fig. 8.8 where the level does not change between 0.8 and 5×10^{17} photons cm^{-2}). CO_3 is expected to form from CO_2 + O, where the O originates from photolysis of another CO_2 molecule into CO + O. With photodesorption hindered, the amount of CO_3 then never exceeds the amount of CO in the ice. In the 20/5.4 N_2/CO_2 experiment, the CO_3 abundance reaches steady state when less than one percent of the CO_2 is converted into CO, which puts a 1% upper limit on the formed CO_3. This is small compared to the ice loss during CO_2 photodesorption experiments, where typically 20% of the ice is lost.

From these results the mass balance photodesorption yield is defined as the CO_2 ice loss yield minus the CO formation yield. Figure 8.9 shows the CO_2, CO and CO_2+CO ice thicknesses in an originally 6.5 ML thick CO_2 ice at 18 K as a function of UV fluence. Practically the photodesorption yield is derived from the slope of the total ice thickness as a function of fluence. This mass balance method of determining the photodesorption yield agrees very well with the yield determined through simultaneous kinetic modeling of bulk photolysis and photodesorption. In Figure 8.9 the CO_2 ice thickness is fitted to a function of the form $A(0) \times e^{-A(1)/\Phi} + A(2) + A(3) \times \Phi$ using the IDL script MPFIT, where Φ is the fluence. The photodesorption yield is determined from $A(3)$. The derived photodesorption yield is the same, within the uncertainties, to the yield derived from

155

fitting a linear function to the CO$_2$+CO ice thickness. This confirms the validity of both methods.
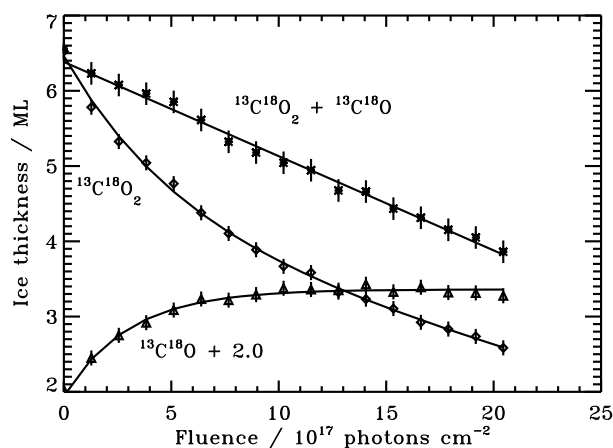

Figure 8.9 – *The CO$_2$ ice thickness as a function of UV fluence (diamonds) plotted together with the formed CO layer thickness (triangles) and the calculated total ice thickness (stars). The CO$_2$ ice loss is fitted as a sum of photolysis (an exponential function) and desorption (a linear function).*

Whichever method is used, the result is a linear coefficient, which gives a photodesorption yield in loss of ice monolayers per 10^{17} UV photons for a 6.5 ML ice at 18 K: 0.27 (ML)/2.1 (10^{17} photons cm^{-2}) = 0.13 ML / (10^{17} UV photons cm^{-2}). This is further converted into a photodesorption yield in CO$_2$ molecules per UV photon (7-10.5 eV): $Y_{\rm pd} = 0.13 \times 10^{-17}$ ML photon^{-1}cm$^2 \times \left(10^{15}$ molecules cm^{-2}/1 ML$\right) = 1.3 \times 10^{-3}$ molecules photon^{-1}.

8.3.2.2 Desorption products

The total photodesorption yield is well constrained from the RAIR spectroscopy of the ice during irradiation. The question remains in which form CO$_2$ ice photodesorbs. Figure 8.10 shows mass spectra acquired during UV irradiation of a 6.2 ML ice at the two temperature extremes, 20 and 60 K. The only visible desorption products are CO and O$_2$, which puts strict upper limits on other potential volatile desorption products. Less volatile species like CO$_2$ (m/z=49 for ^{13}C^{18}O$_2$) cannot be excluded, however, since their cryopumping efficiencies are up to two orders of magnitude higher than for CO. As described in Section 8.2.2 the measured CO QMS signal can be converted into a number of CO molecules desorbed per photon. This number is compared with the total CO$_2$ photodesorption yield to quantify the amount of the CO$_2$ ice that desorbs as CO. From QMS measurements during irradiation experiments, $\sim 20 - 50\%$ desorbs as the fragment CO (Fig. 8.11) and at most 5% as O$_2$. It is thus inferred that more than 50% of the desorbed ice comes off as less volatile species, most likely CO$_2$. This is supported by the fact that the amount of formed CO$_3$ ice is the same whether or not the ice is covered and therefore whether or not photodesorption is allowed. This makes it unlikely that CO$_3$ is photodesorbing in the uncovered experiments. In addition no other C-bearing molecules are formed at significant
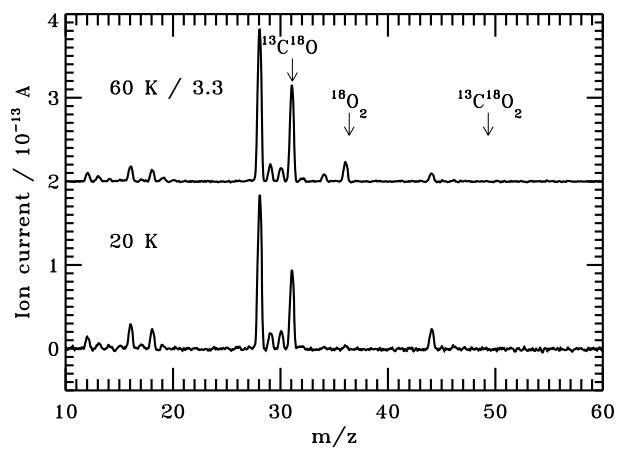
Figure 8.10 – *Mass spectra acquired during irradiation of a 6.2 ML thick $^{13}C^{18}O_2$ ice at 20 and 60 K with a flux of 8.3×10^{13} photons cm^{-2} s^{-1}. The spectra at 60 K have been divided by 3.3 to account for the lower cryopumping of volatiles like CO and O_2 at 60 K compared to at 20 K. In each case the ice is irradiated for 3 hours before acquisition to ensure that the photodesorption rate is stable. Each acquisition lasts 3 hours and consists of ~100 averaged spectra. In addition to photodesorbed ices there are some background CO (m/z=12, 16 and 28), CO_2 (m/z=44) and possibly some background H_2O as well (m/z=18).*
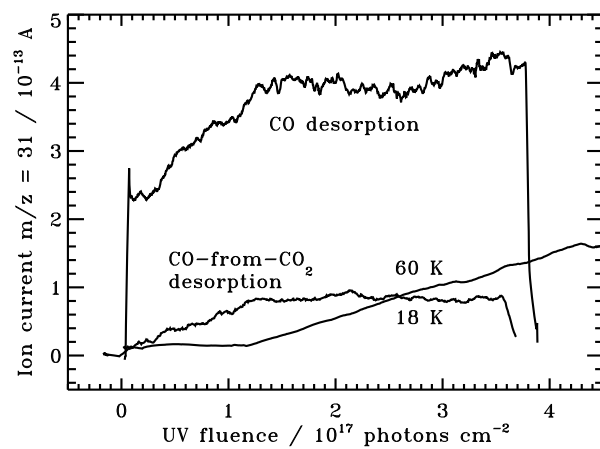
Figure 8.11 – *The detected CO photodesorption during irradiation of a 4 ML $^{13}C^{18}O$ ice at 16 K and $^{13}C^{18}O_2$ ices at 18 K (5.5 ML) and at 60 K (7.4 ML), as a function of UV fluence. The 60 K signal has been divided by 3.3 to account for the lower cryopumping at 60 K compared to 18 K.*

abundances, which only leaves CO_2 as a possible desorption product.

Below we separate the total CO_2 ice photodesorption yield (as measured with RAIRS) from the desorption of CO-from-CO_2 (measured with the QMS). The desorption of CO_2 molecules is taken to be the difference between the total CO_2 ice desorption and the CO-

157

from-CO$_2$ desorption. The total photodesorption quantum efficiency per absorbed UV photon in the surface layer is estimated to 0.4–1 using the lamp spectra from Muñoz Caro & Schutte (2003) and the calibrated UV spectra of CO$_2$ ice from Mason et al. (2006). As seen from the thickness dependence below, this efficiency decreases with depth into the ice.
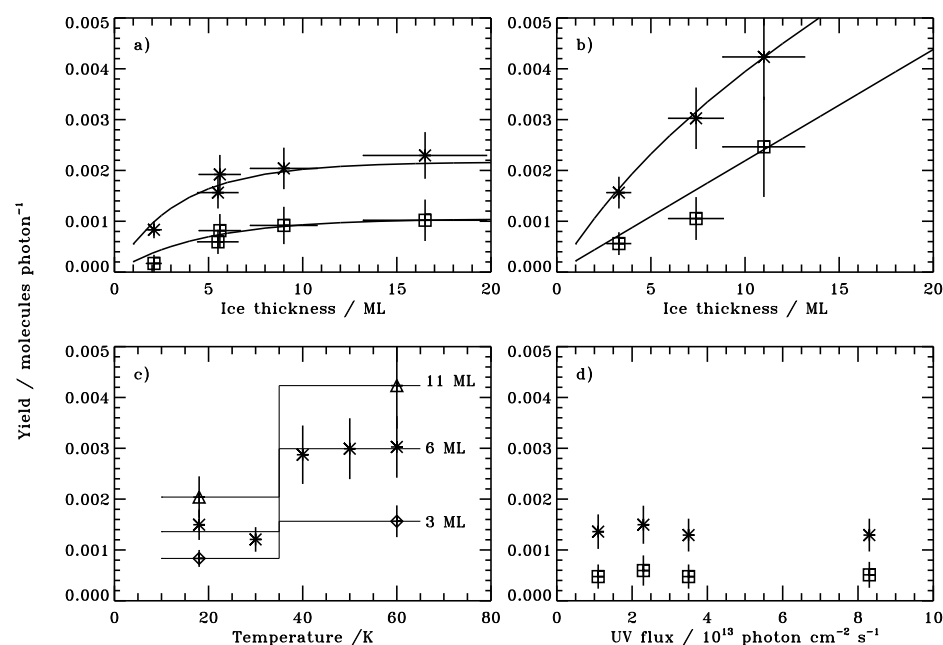
8.3.2.3 Yield dependences on experimental parameters

Figure 8.12 – Total CO$_2$ (crosses) and CO-from-CO$_2$ (squares) photodesorption yield dependences on different parameters. In a) CO$_2$ ices of different thicknesses are irradiated with the same UV fluence of ~6×10^{17} photons cm^{-2} at 18 K and in b) at 60 K. Both the total CO$_2$ and the CO-from-CO$_2$ desorption yields are fitted with functions of the form $c \times (1 - e^{-(x/l)})$ at low temperatures (solid lines), where x is the ice thickness and l an ice diffusion parameter. The two measurements of 5.5 and 5.6 ML ices in a) are from the beginning and the end of a two-month long experimental series. Panel c) shows that the total photodesorption yield is constant with temperature within a low temperature region (<40 K) and within the warmer region 40–60 K for ~3 ML (diamonds), 6 ML (crosses) and 11 ML (triangles) thick ices, irradiated with fluences of ~6×10^{17} photons cm^{-2}. Finally panel d) demonstrates the independence of the total and CO-from-CO$_2$ photodesorption yields on the photon flux for 4–6.5 ML ices at 18 K.

Ice thickness. The total CO$_2$ photodesorption yield at 18 K is thickness dependent up to several monolayers (Fig. 8.12a), which is in contrast with the constant photodesorp-
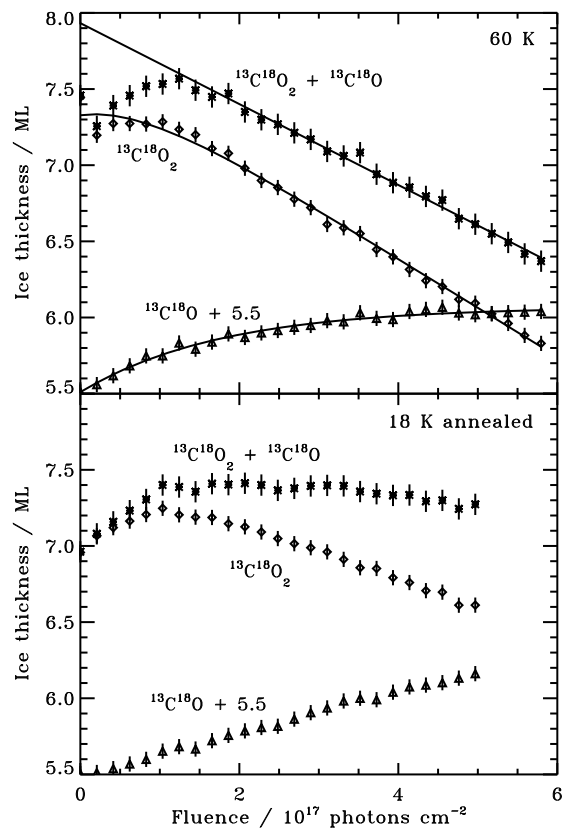
Figure 8.13 – *The top panel shows the measured CO_2 layer thickness (diamonds) of an originally 7.4 ML CO_2 ice at 60 K as a function of UV fluence, plotted together with the formed CO layer thickness (triangles) and the calculated total ice thickness (stars). The CO_2 ice loss is fitted as a sum of photolysis (an exponential function) and desorption (a linear function). The bottom panel shows an 18 K experiment that has been thermally annealed at 60 K prior to irradiation at 18 K. Note the lack of evidence of photodesorption from this ice.*

tion yield of CO reported in Öberg et al. (2007b). The total CO_2 photodesorption yield increases from 8×10^{-4} to 2.3×10^{-3} molecules photon^{-1} when the ice is grown from 2 to 16 ML.

Figure 8.12a also shows simple models fitted to the measured yields of both the CO-from-CO_2 and the total CO_2 photodesorption. The desorption yield of the CO-from-CO_2 is well described by $1.1(\pm 0.2) \times 10^{-3} \times (1 - e^{-(x/4.6(\pm 2.2))})$, where x is the ice thickness in monolayers. The total CO_2 desorption dependence on thickness is a sum of the desorbed CO_2 and CO molecules and is thus modeled as $1.2(\pm 0.1) \times 10^{-3} \times (1 - e^{-(x/2.9(\pm 1.1))}) + 1.1(\pm 0.2) \times 10^{-3} \times (1 - e^{-(x/4.6(\pm 2.2))})$. Both models are fitted using the IDL routine MPFIT. Here the uncertainties only reflect the calculated model errors. As discussed in Section 8.2.2, the total uncertainty is 60%. From these expressions it is clear that more than 90% of the photodesorption events originate in the top 10 ML and 50% in the top 3 ML of the ice. They also expose the thickness dependence of the fraction of the CO_2 desorbing as CO; between 2 and 16 ML this fraction grows from 20 to 45%. The origin of the model and the full significance of the different exponential constants for CO and CO_2 desorption

159

is further discussed below.

The build-up of molecules in the 18 K CO_2 ice is linearly dependent on the ice thickness as expected for a photodesorption yield that is low in comparison to the total ice thickness. In all the ices, ~10% of the original ice is converted to CO and frozen into the CO_2 ice after a typical UV fluence of 5×10^{17} photons cm^{-2}. For comparison ~10% of the original ice is desorbed after the same fluence in a typical 5 ML experiment.

Figure 8.12b shows that the CO_2 photodesorption has a somewhat different thickness dependence at 60 K. The CO-from-CO_2 desorption dependence on thickness is indistinguishable from a linear function and is fitted linearly. The total CO_2 desorption is fitted well, but not uniquely, by $2.2(\pm 0.2) \times 10^{-3} \times (1 - e^{-(x/5.8(\pm 1.2))}) + 2.2(\pm 0.3) \times 10^{-4} \times x$ molecules $photon^{-1}$, where x is the ice thickness in monolayers. This formula indicates that photodesorption takes place deeper into the ice at higher temperatures and that the mean-free-path of CO becomes infinite.

Temperature. At temperatures higher than 30 K the CO_2 photodesorption is initially fluence dependent, which is not the case for colder ices. This is further discussed below; here the constant yield reached after a fluence of 2.0×10^{17} photons cm^{-2} is used for comparison between the photodesorption yields at different temperatures. Figure 8.12c shows the total CO_2 photodesorption yield dependence on temperature for different ice thicknesses. At 18 and 30 K both the total and the CO-from-CO_2 photodesorption yields are indistinguishable within the experimental uncertainties. Between 30 and 40 K the photodesorption yield jumps and above 40 K the photodesorption yield is again independent of temperature.

The build-up of CO molecules in the CO_2 ice is also temperature dependent. Above 30 K, the CO build-up is less than 50% of the build-up at lower temperatures.

Photon flux. Figure 8.12d shows 4–6.5 ML CO_2 ices irradiated with different photon fluxes at 18 K. Between 1.1 and 8.3×10^{13} photons cm^{-2} s^{-1} the CO_2 photodesorption yield in molecules $photon^{-1}$ is constant within the experimental uncertainties. The CO desorbing from the CO_2 ice is independent of the lamp flux as well. At 60 K the ice is irradiated at two different fluxes and, similarly to the colder ice, the photodesorption yield is constant (not shown).

At 18 K, the produced CO ice increases throughout the experiment up to a fluence of $\sim 10 \times 10^{17}$ photons cm^{-2}. After 10×10^{17} photons cm^{-2} the amount of CO ice reaches steady-state, which is only clearly visible in the experiment with the highest fluence. The observed independence of the CO-from-CO_2 photodesorption yield on CO ice content indicates that direct CO photodesorption from the formed CO ice plays a minor role during irradiation of the CO_2 ice.

Time and photon fluence. Figure 8.13 shows the photodesorption of a 60 K, 7.4 ML CO_2 ice irradiated with 2.3×10^{13} photons s^{-1} cm^{-2}. At 60 K there is no measurable photodesorption during the first two hours or a fluence of 2×10^{17} cm^{-2}. This can be compared with the 4.0 ML CO_2 ice at 18 K in Fig. 8.7 (bottom), where photodesorption starts within a fluence of 10^{17} photons cm^{-2}. In the 60 K experiment, the total CO_2 photodesorption yield jumps to 3.0×10^{-3} molecules $photon^{-1}$ after a fluence of 2×10^{17} photons cm^{-2} and remains constant for the remainder of the experiment. This photodesorption delay is observed in all 5–7 ML ices at 40–60 K and also at all thicknesses between 3–11 ML

at 60 K. The QMS measurements also show clear differences between the 18 K and the 60 K experiments (Fig. 8.11). At 60 K, the CO QMS signal is lower than at 18 K during the first 2×10^{17} photons cm^{-2}, corresponding to a yield $\sim 1 \times 10^{-4}$ molecules $photon^{-1}$. After the first 10^{17} photons cm^{-2} the CO signal increases rapidly with fluence.

To test whether this delay in photodesorption onset at 60 K is time or fluence dependent, a 5.8 ML ice is also irradiated at a 50% lower flux. In this experiment the photodesorption according to the RAIRS begins after the same photon fluence, which occurs after twice the amount of time compared with the experiment at a higher flux.

Thermal annealing. In one experiment, a 7.0 ML thick ice is deposited at 60 K and subsequently cooled down to 18 K before starting the irradiation. The CO-from-CO_2 photodesorption yield is $\sim 1 \times 10^{-4}$ $photon^{-1}$, while only an upper limit of 5×10^{-4} $photon^{-1}$ is derived for the total CO_2 photodesorption from the RAIRS measurements. This is significantly lower compared to both unannealed experiments at 18 K and to 60 K experiments (Fig. 8.13). The CO-from-CO_2 QMS signal is similar to that from warm ices during the first 10^{17} photons cm^{-2}. The CO ice build-up, as measured from RAIRS, is similar to the un-annealed ice at 18 K.

8.4 Discussion

8.4.1 CO and N_2 yields and mechanisms

In Öberg et al. (2007b) we concluded that CO photodesorbs from the top one or two ice layers at 15 K. Recent theoretical work shows that CO only desorbs from the absolute surface layer (Takahashi & van Hemert, in prep.), which is supported by the new findings in this study.

The experiments show that the photodesorption of CO depends on thermal annealing, such that annealing at a higher temperature results in a lower desorption yield. The annealing most likely results in a more compact ice with a smaller effective surface area as well as stronger bound molecules. These two effects then add up to decrease the quantum efficiency of the photodesorption process. The reason for the linear dependence with temperature is unclear and may be coincidental. This behavior cannot be extrapolated to lower temperatures, since a 15 K ice should be amorphous.

The new photodesorption experiments with N_2 further constrain the CO photodesorption mechanism. Consistent with Öberg et al. (2007b) there is no evidence of direct N_2 photodesorption. The increase in photodesorption yield of N_2 when mixed with CO or grown in a monolayer on top indicates that ~5% of the UV photon absorptions of CO molecules result in the desorption of a neighboring molecule rather than the desorption of the originally excited molecule. The decreasing CO photodesorption in the mixed ice and the lack of initial CO desorption in the layered experiment also confirm that CO only desorbs from the top ice layer.

161

8.4.2 The CO_2 yield and mechanism

In contrast to CO and H_2O photodesorption (Andersson et al. 2006; Andersson & van Dishoeck 2008, Takahaski & van Hemert, in prep.), the photodesorption mechanism of CO_2 has not been theoretically addressed yet. From the dependencies reported here, the mechanism may be constrained, however, and it is similar to that of H_2O. CO_2 photodissociates to CO+O, where the products have excess energy. This is followed by both reactions in the ice to form the observed CO_3, and recombination to CO_2. Some of these reaction products subsequently desorb.

The flux independence of the CO_2 photodesorption has also previously been seen for H_2O and CO ices (Westley et al. 1995b; Öberg et al. 2007b, Öberg et al. accepted by ApJ). This independence is expected for single photon processes, but not for multi photon processes or desorption induced by excess heat from the lamp. This is consistent with the suggested mechanism of dissociation fragments and recombined molecules traveling through the ices before desorbing.

The CO_2 photodesorption yield is clearly thickness dependent, which is in contrast to the CO photodesorption from surfaces only. This difference can be understood from the fact that before a desorption event occurs, the CO_2 molecule is dissociated into energetic products (whether concerned with the fragments or recombined molecules), which may travel through several monolayers of ice before they are quenched by the surrounding matrix. Assuming a homogeneous ice, the probability of a molecule with excess energy, from dissociation or recombination, reaching the ice surface and desorbing is only dependent on the excess energy, the diffusion properties of the molecule and the ice depth at which it receives its excess energy. The diffusion properties of a molecule are simplest described by the average distance the molecule travels through the ice before being stopped. Defining l as the average distance traveled by a molecule before quenched by the surrounding ice, the fraction of particles with excess energy that will move through a slab of ice of thickness x is expected to be proportional to $e^{-x/l}$, assuming uniform photochemistry throughout the ice and that the direction the molecule travels is independent of ice depth. Integrating over the ice depth from 0 to x, the total desorption of particles between 0 and x is then proportional to $1 - e^{-x/l}$.

We find that this type of expression describes the photodesorption at low temperatures well, with an average travel distance or mean-free-path of 2.9 ML for the CO_2 photodesorption and 4.6 ML for the CO fragment desorption. The two different values for the mean-free-paths have large uncertainties and it is not clear that the difference is significant. The values are however consistent with the different sizes of CO and CO_2, since the larger molecule is expected to be less mobile in the ice. The different mean-free-paths may also be partly due to different mechanisms, i.e. dissociation versus recombination, through which the CO fragment and the recombined CO_2 molecule receive excess energy.

The different mean-free-paths for CO and CO_2 desorption from CO_2 ice can also be consistent with a different desorption mechanism of CO_2 molecules – momentum transfer to a surface CO_2 molecule from a smaller fragment originating in an underlying layer. This is observed in simulations by Andersson & van Dishoeck (2008) as an equally important photodesorption pathway for H_2O compared to desorption of the re-

combined molecule. The ice thickness dependence of this kind of process remains to be explored, since it requires more complex models than the simple mean-free-path model presented here.

Other desorption pathways of the CO fragment can however be ruled out from the experiments presented here. The desorbed CO molecules do not originate in photodesorption of CO ice, since the yield does not increase with an increasing fraction of CO in the ice – this fraction never reaches equilibrium during most low temperature experiments – while the CO QMS signal does. In addition, the underlying substrate seems to have no influence on the desorption yield; hence substrate mediated processes are excluded as well.

At temperatures above the pure CO desorption temperature of ~30 K, the increased photodesorption yield is most likely due to the increased mobility of CO_2 and CO in the ice. This is seen from the longer mean-free-path for desorbing CO_2 molecules and the infinite mean-free-path of CO. The latter points to a very high mobility of CO in the ice at these temperatures, which results in that most of the produced CO thermally desorbs once formed through CO_2 dissociation. It is also shown by the onset of O_2 photodesorption (Fig. 8.10). The desorption of O_2 is less than CO at any temperature (Section 8.3.2.1), but its mere presence shows that at 60 K oxygen atoms are very mobile and produced abundantly.

A curious and not yet fully understood feature is the delayed onset of both CO and CO_2 photodesorption from CO_2 ices at 40–60 K. Since it is a fluence rather than a time effect it is probably due to a re-structuring of the ice induced by UV irradiation. This restructuring is indicated by a change in the infrared spectral profile (not shown), which seems more pronounced for the warmer ices compared to the colder ones. This proposed re-structuring may also be responsible for the apparent initial increase in CO_2 in Fig. 8.13. Ice band strengths depend on ice structure (e.g. Öberg et al. 2007a) and this increase in CO_2 signal is most likely due to structural changes upon UV irradiation, modifying the strength of the CO_2 ice band, rather than more CO_2 molecules adsorbing. Similar changes in band strength have been previously observed in CO and in H_2O ices bombarded by ions (Loeffler et al. 2005; Gomis et al. 2004)

The importance of ice structure for the photodesorption yield is seen for CO as well, as discussed above. For CO_2 this importance is further shown by the experiment on a thermally annealed ice, where the photodesorption yield is < 40% of the yield of an amorphous ice. This is in contrast with the increased photodesorption yield for warm (40–60 K) ices, which are expected to have similar ice structures as the annealed ice. This new ice structure probably has a smaller effective ice surface compared to the 18 K amorphous ice, explaining the low photodesorption yield of the annealed ice. At temperatures above 40 K this decrease in surface does not affect the yield due to the high mobility of molecules in the ice. In summary, the CO_2 photodesorption yield is both temperature and structure dependent.

8.4.3 Astrophysical significance

8.4.3.1 CO and N$_2$

The relevance of CO photodesorption at 15 K is discussed in detail in Öberg et al. (2007b). The results here show that the previously reported yield is dependent on temperature and annealing between 15 and 27 K. The astrophysical significance of this dependence is probably limited, however. Because the desorption temperature and annealing temperature are similar, only a minor fraction of the pure CO ice will ever be annealed in astrophysical environments. Therefore the photodesorption yield derived at 15 K may be used for most purposes, also where a real temperature gradient exists.

While a temperature gradient may not significantly reduce the CO photodesorption yield, a layer of N$_2$ ice on top of the CO ice does. This layer may form either through later freeze-out or through selective photodesorption as shown in the experiments. Because of the peculiar photodesorption mechanism of CO ice, this study shows that a single monolayer of N$_2$ ice initially reduces the CO photodesorption yield with more than 80%. After a UV fluence of 8.5×10^{17} photons cm^{-2} (corresponding to ~300 years of irradiation at cloud edges and ~3 million years in cloud cores), the yield has increased to 25% of the pure CO ice photodesorption yield, indicating that 25% of the N$_2$ layer is desorbed. This probably happens through CO co-desorption, since the photodesorption yield of pure N$_2$ is too low to account for the observed desorption. N$_2$ co-desorption is also observed in a mixed CO:N$_2$ ice where N$_2$ photodesorbs at a yield of 3×10^{-4} photon^{-1}. This is still a very low photodesorption yield compared to e.g. the CO photodesorption yield and its astrophysical significance is doubtful. Other non-thermal desorption mechanisms such as cosmic ray induced spot heating will likely be more important.

8.4.3.2 CO$_2$

At low temperatures and for thick ices the CO$_2$ photodesorption yield is $2.3(\pm 1.4) \times 10^{-3}$ photon^{-1}, which is almost identical to the CO photodesorption yield. Of the desorbed ice more than 50% desorbs in the form of CO$_2$, while the remaining 20–50% desorbs as CO. At higher temperatures some CO$_2$, up to 5%, also desorbs as O$_2$. This means that similar CO$_2$ and CO abundances are expected in regions where photodesorption dominates, assuming that the photodesorption yields of the two molecules are not much different for astrophysical ice morphologies compared to the pure ices studied here. This remains to be investigated, especially for the astrophysically relevant cases of CO ice on top of CO$_2$ ice, and CO:CO$_2$ and CO$_2$:H$_2$O mixtures (Pontoppidan et al. 2008). Based on our results we expect the recombined and thus energetic CO$_2$ molecule to penetrate at least as many CO ice layers during photodesorption as the 10 ML of CO$_2$ ice observed in this study, since CO forms a more loosely bound ice compared to CO$_2$. The behavior of CO$_2$ in a H$_2$O matrix is more difficult to predict. Hence, until such a laboratory study exists we recommend to use the equation presented here for CO$_2$ photodesorption, with the possible modification of taking into account that only a fraction of the ice is CO$_2$ ice.

In the regions in clouds and disks where ices begin to form, the ice thickness dependence of the CO$_2$ photodesorption needs to be taken into the account. As soon as the grain

is covered with less than 10 ML of CO_2 ice, the CO_2 photodesorption yield decreases considerably with ice thickness according to $1.2 \times 10^{-3} \times (1 - e^{-x/2.9}) + 1.1 \times 10^{-3} \times (1 - e^{-x/4.6})$ at 18 K, where x is the ice thickness and the two parts in the yield expression are due to CO_2 and CO desorption, respectively, during the irradiation of a CO_2 ice.

Heated or thermally annealed, i.e. heated and subsequently cooled down, CO_2 ice is observed toward many high- and low-mass protostars (Gerakines et al. 1999; Pontoppidan et al. 2008). Because of the irreversibility of the infrared spectroscopic signature of heated CO_2 ice, the two cannot be easily distinguished. At temperatures higher than the pure CO sublimation line at 25–30 K, the CO_2 photodesorption yield increases to $2.2 \times 10^{-3} \times (1 - e^{-x/5.8}) + 0.22 \times 10^{-3} \times x$ molecules photon^{-1} for the CO_2 and the CO-fragment desorption, respectively. This results in a CO_2 yield increase of at most a factor of two. In addition, possible annealing may decrease the photodesorption yield to a value that is less than 40% of the cold amorphous CO_2 ice yield. The uncertainty in the photodesorption yield is thus an additional factor of 2–3 in thermally processed regions.

8.4.3.3 CO_2 astrophysical model

CO_2 is not detected directly in the radio regime due to its lack of a permanent dipole moment. It is instead traced by HCO_2^+ toward e.g. the protostar L 1527 IRS. As a test case we use a simple model to investigate whether the recently observed HCO_2^+ toward L 1527 IRS may be explained by photodesorption of CO_2 ice. Sakai et al. (2008) estimated the gas phase CO_2 abundance to be $> 2.9 \times 10^{-7}$ with respect to H_2, by using a simple reaction scheme for the CO_2 to HCO_2^+ chemistry and assuming that the CO_2 is extended over the beam size of the IRAM 30 m telescope. Furlan et al. (2008) report a CO_2 ice abundance of 5×10^{-6} with respect to H_2 in L 1527 IRS, which is used in our model. This abundance is almost an order of magnitude lower than what is observed toward a large sample of low-mass protostars (Pontoppidan et al. 2008) and may be underestimated. The effect of increasing the CO_2 fractional abundance to $\sim 3 \times 10^{-5}$ is discussed below.

To simplify the calculation we assume that the average temperature is below 30 K and that the hydrogen density is constant throughout the envelope. At this low temperature thermal desorption of CO_2 is negligible and therefore the equilibrium gas phase abundance of CO_2 is dependent only on the UV photodesorption and the freeze-out rates. We also make the approximation that the total CO_2 abundance is constant throughout the envelope, since observations show that CO_2 forms in ices at the edges of clouds and does not increase deeper into the cloud (Pontoppidan 2006). The UV field is composed of the interstellar radiation field of 10^8 photons cm^{-2} s^{-1}, which is attenuated with A_V, and the UV photons produced inside the cloud by cosmic rays. For a typical galactic cosmic ray flux, the resulting UV photon flux is of the order of 10^4 photons cm^{-2} s^{-1} with a factor of 3 uncertainty (Shen et al. 2004). Using our derived photodesorption yields and the estimated freeze-out rate of CO_2 we calculate the steady-state gas abundance of CO_2 as a function of A_V for small and large grains.

The photodesorption rates of CO_2 molecules from grain surfaces in molecules s^{-1} due to external and cosmic ray induced UV photons, respectively, is described by

$$R_{\text{PD-ISRF}} = I_{\text{ISRF-FUV}} e^{-\gamma A_v} Y_{\text{pd}} \left(\pi a_{\text{gr}}^2 \right), \tag{8.2}$$

$$R_{\text{PD-CR}} = I_{\text{CR-FUV}} Y_{\text{pd}} \left(\pi a_{\text{gr}}^2 \right), \tag{8.3}$$

$$Y_{\text{pd}} = 0.0012(1 - e^{-x/2.9}), \tag{8.4}$$

$$x = n_{CO_2-\text{ice}} / \left(1 \times 10^{15} \times \pi a_{\text{gr}}^2 n_{\text{gr}} \right), \tag{8.5}$$

and

$$n_{CO_2-\text{ice}} = 5 \times 10^{-6} n_{\text{H}} - n_{CO_2-\text{gas}}, \tag{8.6}$$

where $I_{\text{PD-ISRF}}$ is the strength of the external irradiation field with energies 6-13.6 eV and $I_{\text{PD-FUV}}$ is the strength of the UV field due to cosmic rays. γ is a measure of UV extinction relative to visual extinction, which is ~2 for small interstellar grains and <0.6 for grains of a few μm (Roberge et al. 1991; van Dishoeck et al. 2006), and a_{gr} is the grain radius. Y_{pd} is the experimentally determined CO_2 photodesorption yield for temperatures below 30 K (Eq. 8.4). x is the ice thickness in monolayers, which is defined in terms of the CO_2 ice abundance ($n_{CO_2-\text{ice}}$ in cm^{-3}), grain surface ($\pi a_{\text{gr}}^2 n_{\text{gr}}$ in cm^2 cm^{-3}) and amount of molecules per monolayer (1×10^{15} cm^{-2}) in Eq. 8.5. Equation 8.6 states the relationship between the gas and ice phase CO_2 abundances ($n_{CO_2-\text{gas}}$ and $n_{CO_2-\text{ice}}$) when the total CO_2 abundance is $5 \times 10^{-6} n_{\text{H}}$ and n_{H} is set to 1×10^4 cm^{-3}.

The accretion rate of CO_2 molecules R_{acc} is a product of the molecular velocity, the grain surface, the sticking coefficients and the gas phase abundance of CO_2 according to

$$R_{acc} = -4.57 \times 10^4 \left(\frac{T}{m_{CO_2}} \right)^{\frac{1}{2}} \left(\pi a_{gr}^2 \right) S \, n_{CO_2-gas}. \tag{8.7}$$

In Eq. 8.7 the gas temperature T is set to 10 K, m_{CO_2} is the CO_2 mass in atomic mass units, and S is the sticking coefficient, which is assumed to be 1 (Bisschop et al. 2006).

At steady-state the total photodesorption rate (i.e. the sum of Eqs. 8.2 and 8.3) is equal to the accretion rate. Figure 8.14 shows the resulting steady-state CO_2 gas phase abundance as a function of A_{V} for small classical 0.1 μm grains and after grain growth to a few μm. At A_{V} <3 mag, CO_2 gas is photodissociated and the model is not valid there. Deep into the envelope, the gaseous CO_2 abundance due to cosmic ray induced photodesorption is ~ 2×10^{-8}, which is about an order of magnitude lower than the observed CO_2 abundance. For small grains the external UV light also probably does not penetrate deep enough into the envelope to increase the average abundance significantly. On average about 1% of the total CO_2 abundance is kept in the gas phase through photodesorption. If the CO_2 ice abundance is increased to ~ 3×10^{-5}, the CO_2 gas abundance increases by an order of magnitude at low extinctions. Deep into the cloud the abundance only increases by a factor of two, since the photodesorption rate only depends on the ice thickness up to ~10 ML. In cloud and envelope material dominated by small grains, photodesorption

probably does not explain gaseous CO_2 abundances of 5–10%, as observed toward L 1527 IRS, unless there is a strong internal UV source and the UV is scattered into the cavities created by the outflow (Spaans et al. 1995) where it can photodesorb material in the cavity walls. Indeed, L1527 IRS is well known for its prominent outflow and X shaped cavity wall on scales comparable to the IRAM 30m beam (MacLeod et al. 1994; Hogerheijde et al. 1998).

In disks, or in general where grain growth has occurred, the picture changes dramatically. Millimeter observations of outer disks show grain growth up to mm size (Rodmann et al. 2006; Lommen et al. 2007), and the UV irradiation may then penetrate deep into the disk releasing a high fraction of the CO_2 ice into the gas phase. At an A_V of 10 mag the CO_2 fractional abundance is now $\sim 1\times10^{-6}$ or 20% of the total CO_2 abundance. Similarly to the case with small grains, increasing the CO_2 ice abundance only increases the CO_2 gas abundance substantially at low extinctions.

This simple model thus shows that the experimentally determined CO_2 photodesorption yield is high enough to release large amounts of CO_2 ice into the gas phase if moderate grain growth has occurred. Even with small grains and no internal UV source except that produced by cosmic rays, photodesorption may keep up to ~1% of the total CO_2 abundance in the gas phase deep into cloud cores. This model stresses, once again, that photodesorption of ices needs to be taken into account when modeling gas-grain interactions.
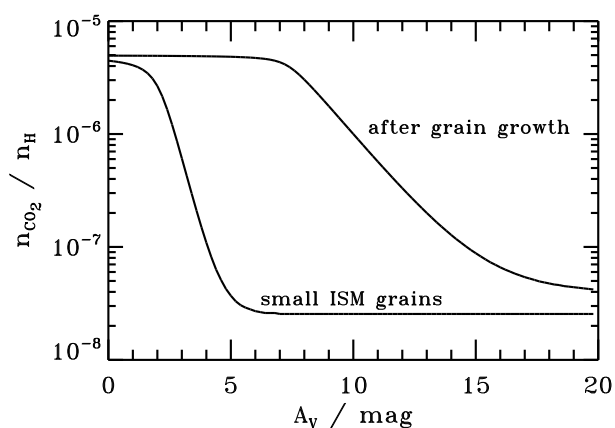

Figure 8.14 – *The CO_2 gas phase abundance with respect to the total hydrogen ($H+H_2$) column density assuming a total (gas + ice) CO_2 abundance of 5×10^{-6}. The two tracks assume classical 0.1 μm grains and grain growth up to a few μm, respectively.*

8.5 Conclusions

1. The CO photodesorption yield is temperature dependent between 15 and 27 K, which is described empirically by $2.7 \times 10^{-3} - (T - 15) \times 1.7 \times 10^{-4}$ molecules photon^{-1}. The anti-correlation between yield and temperature is probably due to ice re-structuring into a more compact configuration – the observed linearity may be coincidental, however. For most astrophysical applications the yield measured at 15 K is appropriate to use.

2. The CO photodesorption is initially reduced by more than 80% when the CO ice is covered by 1 ML of N_2 ice and decreases with UV fluence when mixed with N_2 due to surface build-up of N_2 ice, confirming that CO only desorbs from the ice surface.

3. N_2 co-desorbs with CO at 16 K in an ice mixture and in a layered ice with a yield of 3×10^{-4} molecules photon^{-1}.

4. A CO_2 photodesorption event starts with the photodissociation of a CO_2 molecule into CO and O. The fragments either desorb directly or react and recombine to form CO_2 and CO_3 before desorbing. The CO_3 yield is however less than 1% and the two main desorption products are CO and CO_2.

5. The CO_2 photodesorption yield is thickness dependent at all temperatures between 18 and 60 K. At 18–30 K the yield is well described by $1.2 \times 10^{-3} \times (1 - e^{-x/2.9}) + 1.1 \times 10^{-3} \times (1 - e^{-x/4.6})$, and at 40–60 K by $2.2 \times 10^{-3} \times (1 - e^{-x/5.8}) + 0.22 \times 10^{-3} \times x$ molecules photon^{-1}, where x is the ice thickness in monolayers. The first part in each yield equation is due to desorbing CO_2 molecules and the second part to desorbing CO molecules.

6. The thickness dependence of CO_2 photodesorption is understood from a mean-free-path perspective, where the different excited fragments travel a different average distance through the ice before being stopped. At higher temperatures, this mean free path increases due to increased mobility of molecules in the ice.

7. A simple model of an envelope using the observed CO_2 abundance in L 1527 IRS shows that CO_2 photodesorption can maintain CO_2 fractional abundances up to 1×10^{-6} in the gas phase at $A_V \sim 10$ mag after moderate grain growth and $2-3 \times 10^{-8}$ using small ISM grains. At lower extinctions the photodesorption is higher due to the external irradiation field and a high fraction of the total CO_2 ice abundance is maintained in the gas phase.